

Abstract

The accuracy of surface deformation derived from Interferometric Synthetic Aperture Radar (InSAR) observations depends on the quality of the chosen interferogram subset. We present a method to select interferogram subsets based on unwrapping errors rather than temporal baseline thresholds. Using Sentinel-1 interferograms over the Tulare Basin (CA), we show that tropospheric noise dominates short temporal baseline subset solutions (with up to 2.9 cm/yr residuals at co-located GPS sites), while decorrelation leads to a systematic underestimation of true deformation rate in long temporal baseline subset solutions (with up to 5.5 cm/yr residuals). Our new workflow better mitigates these two noise sources at the same time. In the Eagle Ford (TX) region, our strategy revealed up to ~ 11 cm of cumulative line-of-sight (LOS) deformation over a ~ 900 km² region. This deformation feature is associated with ongoing oil and gas activities and is reported for the first time here.

Plain Language Summary

Deformation estimates are often impacted by noise related to weather conditions and surface vegetation changes. It is common to select an interferogram subset based on a temporal baseline threshold. However, InSAR phase quality may be influenced by other factors such as the weather conditions and surface vegetation rather than temporal baselines. We designed an InSAR processing strategy and applied it to two vegetated regions that experience land subsidence due to agriculture groundwater pumping or oil and gas production. In the Tulare Basin, we showed that deformation estimates are impacted by weather and vegetation related noise and can vary substantially depending on which interferograms are chosen. With our strategy, we better mitigate both noise sources at the same time. In the Eagle Ford region, our workflow revealed up to ~ 11 cm of surface deformation over a ~ 900 km² area for the first time. This is an oil and gas producing region where production activities have led to an increase in seismicity. Based on these findings, accurate surface deformation derived from InSAR data is now achievable in densely vegetated regions and can play an important role in future induced seismicity studies.

1 Introduction

Interferometric Synthetic Aperture Radar (InSAR) is an imaging radar technique for measuring surface deformation associated with geophysical processes including, but not limited to, tectonics (e.g., Fialko et al., 2002; Wright et al., 2004; Shirzaei & Bürgmann, 2013; Fielding et al., 2017; Xu et al., 2021), volcanism (e.g., Jónsson et al., 2000; Pritchard & Simons, 2002; Hooper et al., 2004; Lundgren et al., 2013), and groundwater hydrology (e.g., Amelung et al., 1999; Hoffmann et al., 2001; Schmidt & Bürgmann, 2003; Bell et al., 2008; Chaussard et al., 2014). Achieving millimeter-to-centimeter level accuracy required by many of these studies, however, is challenging due to effects such as decorrelation and atmospheric artifacts. Physical changes in the surface properties between two radar image acquisitions (e.g., vegetation growth and surface disturbance) lead to phase decorrelation (H. A. Zebker & Villasenor, 1992). Phase measurements at completely decorrelated radar pixels do not contain spatially coherent phase information. Conversely, changes in temperature, pressure, and humidity (Bevis et al., 1992) often appear as spatially coherent tropospheric noise, similar to surface deformation signals. While weather models and topography data can be used to estimate and remove the stratified tropospheric noise component (e.g., Doin et al., 2009; Wadge et al., 2002; Jolivet et al., 2011; Li et al., 2009; Bekaert et al., 2015a, 2015b), these approaches often fail to capture the turbulent noise component that is approximately random at time scales greater than a day (Emardson et al., 2003). In many InSAR studies, decorrelation and tropospheric turbulence noise are the two major factors that limit InSAR measurement accuracy.

65 To mitigate tropospheric and decorrelation noise, Berardino et al. (2002) developed
 66 the Small BAseline Subset (SBAS) method to derive surface deformation solutions from
 67 a stack of interferograms. The algorithm assumes that interferograms with large tem-
 68 poral baselines (the time between two radar acquisitions used to form the interferogram)
 69 often suffer from more severe decorrelation artifacts. Therefore, the use of a temporal
 70 baseline threshold in the subset selection can reduce the number of decorrelated phase
 71 measurements used in surface deformation analysis. A problem arises in areas with dense
 72 vegetation where phase decorrelation occurs even in short baseline interferograms (e.g.,
 73 48 or 60 days), which limits the interferogram subset size and ability to reduce other noise
 74 terms. To better mitigate decorrelation noise, Persistent Scatterer (PS) algorithms were
 75 developed to select pixels that suffer from minimal decorrelation artifacts (e.g., roads,
 76 buildings, or bare rock) (e.g., Ferretti et al., 2000; Hooper et al., 2004; Agram, 2010; Huang
 77 & Zebker, 2022; Wang & Chen, 2022). In areas with severe decorrelation, only phase mea-
 78 surements at PS pixels are suitable for surface deformation analysis. To further advance
 79 the capability of PS interferometry, Ferretti et al. (2011) jointly analyzed nearby pix-
 80 els (Distributed Scatterers) with homogeneous amplitude distributions (referred to as
 81 statistically homogeneous pixels or SHP). The InSAR phase observations from each SHP
 82 group are averaged to improve the signal-to-noise-ratio (SNR) and a covariance matrix
 83 model (Guarnieri & Tebaldini, 2008) is employed to filter phase measurements for sur-
 84 face deformation analysis.

85 While different selection criteria are adopted in existing PS/DS algorithms, they
 86 often require InSAR phase measurements to remain stable at the identified PS/DS over
 87 the entire InSAR observation period. However, even at relatively stable PS/DS pixels,
 88 phase measurements are often decorrelated in a portion of the interferograms. It is com-
 89 mon to assume interferograms with longer temporal baselines tend to decorrelate more
 90 than interferograms with shorter temporal baselines. However, other factors (e.g., weather
 91 and surface conditions) may cause decorrelation as well. Based on these observations,
 92 we design a processing strategy that selects an interferogram subset for surface defor-
 93 mation analysis based on decorrelation and the associated phase unwrapping errors, re-
 94 gardless of interferogram temporal baselines. This new workflow allows us to enhance
 95 phase coherence and reduce decorrelation noise through an optional step that integrates
 96 recent phase reconstruction algorithms (e.g., Guarnieri & Tebaldini, 2008; Fornaro et al.,
 97 2015; Ansari et al., 2018). This InSAR processing strategy is computationally efficient
 98 and easy to implement, and can be incorporated into existing workflows to extend the
 99 use of the Small BAseline Subset approaches over densely vegetated areas.

100 2 Methodology

101 Interferometric Synthetic Aperture Radar (InSAR) techniques compute the phase
 102 difference between two SAR images over the same area of interest. After removing the
 103 phase component related to surface topography, the observed InSAR phase at a pixel
 104 of interest, $\Delta\phi$, can be written as (Hanssen, 2001):

$$\Delta\phi = \frac{4\pi}{\lambda} \Delta d_{LOS} + \Delta\phi_{orb} + \Delta\phi_{decor} + \Delta\phi_{unwrap} + \Delta\phi_{dem} + \Delta\phi_{iono} + \Delta\phi_{tropo} + \Delta\phi_n \quad (1)$$

105 where λ is the radar wavelength and Δd_{LOS} is the surface deformation between
 106 two SAR acquisition dates along the radar line-of-sight (LOS) direction. The remain-
 107 ing phase terms on the right are InSAR measurement noise due to orbital errors, phase
 108 decorrelation and associated unwrapping errors, digital elevation model (DEM) errors,
 109 ionospheric and tropospheric artifacts, and other smaller residual noise terms such as ther-
 110 mal or soil moisture effects. Among these noise terms, orbital errors, DEM errors, and
 111 ionospheric delays can be corrected during the interferogram formation (e.g., Fattahi &
 112 Amelung, 2013; Fattahi et al., 2017). Additionally, stratified tropospheric noise can be

113 estimated and removed using a combination of global or local atmospheric weather mod-
 114 els along with zenith tropospheric delay measurements at GNSS sites (e.g., the GACOS
 115 correction as described in Yu et al. (2017)). Therefore, our algorithm design focuses on
 116 the reduction of decorrelation and the associated phase unwrapping errors (H. A. Zebker
 117 & Villasenor, 1992) as well as tropospheric turbulence noise errors (e.g., H. A. Zebker
 118 et al., 1997; Emdarson et al., 2003).

Given N high-quality interferograms derived from M SAR acquisitions, Berardino et al. (2002) proposed a method to solve for the surface deformation time series at a pixel of interest as:

$$Bv = \Delta\Phi \quad (2)$$

119 where $v = [v_1, \dots, v_{M-1}]^T$ is the vector of unknown mean velocities between each con-
 120 secutive SAR acquisition, and $\Delta\Phi = [\Delta\phi_1, \dots, \Delta\phi_N]^T$ is a $N \times 1$ vector of observed In-
 121 SAR phases at the given pixel. B is the $N \times (M-1)$ system matrix as defined in (Berardino
 122 et al., 2002), and we can solve for v as an inverse problem of Equation (2).

123 Berardino et al. (2002) named this InSAR time series analysis algorithm the Small
 124 BAseLine Subset (SBAS) method because a subset of N high-quality InSAR observations
 125 is chosen for the time series inversion based on user-defined temporal and spatial base-
 126 line thresholds (Fig. 1, left). The algorithm was designed based on the fact that inter-
 127 ferograms with large temporal or spatial baselines are more likely to suffer from more
 128 severe decorrelation noise. Thus, selecting a subset of interferograms with small base-
 129 lines allows users to limit the total number of decorrelated phase measurements in the
 130 InSAR phase vector Φ in Equation (2). By contrast, tropospheric turbulence noise is not
 131 correlated with temporal or spatial baselines (e.g., Tymofeyeva & Fialko, 2015; M. S. Ze-
 132 bker et al., 2023). Because tropospheric turbulence noise can be considered spatially co-
 133 herent (similar to deformation signals) but random in time between SAR acquisitions
 134 (Emdarson et al., 2003), it is desirable to include a large number of interferograms ac-
 135 quired on different dates (especially those with long temporal baselines and thus larger
 136 secular deformation signals) as input data for the SBAS inversion (Supporting Informa-
 137 tion S1).

138 One limitation of the SBAS approach is that the InSAR decorrelation noise level
 139 cannot be measured using temporal and spatial baseline alone. In areas with dense veg-
 140 etation, a short temporal baseline threshold (e.g., 48 or 60 days) is often imposed to limit
 141 temporal decorrelation noise due to vegetation growth in the interferogram subset. How-
 142 ever, this leads to a substantial reduction in the total number of phase observations used
 143 in time series inversion, which limits our ability to mitigate tropospheric noise (e.g., H. A. Ze-
 144 bker et al., 1997; Zheng et al., 2021) and closure phase biases (e.g., Ansari et al., 2021;
 145 Zheng et al., 2022). A small portion of interferograms with longer temporal baselines (e.g.,
 146 a year) often maintain good phase coherence at certain stable pixels such as roads, man-
 147 made structures, and barren terrain. These phase observations can improve the accu-
 148 racy of the SBAS surface deformation estimates. Based on these facts, our new work-
 149 flow is designed to choose the interferogram subset based on the phase quality of the in-
 150 terferogram, rather than temporal and spatial baseline thresholds (Fig. 1, right). To do
 151 this, we first form all possible interferogram pairs. If severe decorrelation noise is present,
 152 we enhance InSAR phase quality through phase reconstruction methods such as coherence-
 153 based filtering (e.g., Guarnieri & Tebaldini, 2008; Ferretti et al., 2011; Fornaro et al., 2015;
 154 Mirzaee et al., 2023) or an interpolation between phase observations at stable PS pix-
 155 els (e.g., Ferretti et al., 2000; Hooper et al., 2004; Agram, 2010). This increases the to-
 156 tal number of interferograms suitable for the time series analysis. The reconstructed
 157 interferograms are then unwrapped. Finally, we compute the amount of unwrapping er-
 158 rors for each interferogram and choose a subset of interferograms with small total phase
 159 unwrapping errors as input for the time series inversion. For each unwrapped interfer-
 160 ogram, we define the phase unwrapping error at a pixel m as:

$$\phi_m^{err} = \sum_k^4 \Delta\phi_{mn}, \text{ if } \Delta\phi_{mn} > \pi \quad (3)$$

161 where $\Delta\phi_{mn}$ is the unwrapped phase difference between pixel m and n in an interferogram, and pixel n is one of four adjacent pixels to center pixel m . If $\Delta\phi_{mn} < \pi$, the
 162 unwrapping error contribution is 0, as defined in C. Chen and Zebker (2001). We compute
 163 the total phase unwrapping error of an interferogram as the sum of the phase un-
 164 wrapping error over all radar pixels (Wang & Chen, 2022).
 165

166 3 Test Sites and Data Processing

167 Our first study site is the Tulare Basin in the southern portion of the Central Val-
 168 ley, California (Fig. S1, left), a large agricultural region that has relied on groundwa-
 169 ter since the early 1920s (Poland, 1975). The groundwater demand in combination with
 170 extended droughts throughout California has led to aquifer sediment compaction and
 171 subsequent land subsidence (e.g., Galloway et al., 1999; Faunt et al., 2016). As a result,
 172 InSAR techniques have been used to monitor pumping-induced land subsidence and es-
 173 timate permanent groundwater loss in the region (e.g., Farr & Liu, 2015; Smith et al.,
 174 2017; Ojha et al., 2018; Neely et al., 2021). Our second study site is in Central Texas
 175 and contains a portion of the Eagle Ford Shale, southeast of the San Antonio-Austin metro-
 176 plex (Fig. S1, right). The Eagle Ford Shale is a large oil-producing region. The recent
 177 ramp-up in shale fracking activities led to increased reliance on groundwater resources
 178 from the Carrizo-Wilcox aquifer that overlays the Eagle Ford Shale (Scanlon et al., 2020).
 179 This combination of groundwater withdrawal and oil and gas production can produce
 180 complex deformation signals. The growth of vegetation at both of these sites can lead
 181 to severe decorrelation in interferograms with relatively short temporal baselines (e.g.,
 182 ~ 2 months), a challenging scenario for InSAR time series analysis. Furthermore, be-
 183 cause both sites are located in the mid-latitude and are relatively flat regions, DEM and
 184 ionospheric noise terms are not substantial. Given that the primary noise terms are tropo-
 185 spheric turbulence noise and decorrelation, we chose these two sites to demonstrate
 186 the advantages of our time series analysis workflow.

187 For the California case, we processed 122 C-Band Sentinel-1 SAR images (path 137,
 188 frame 114) acquired between 2017 and 2021 using a geocoded single-look-complex (SLC)
 189 algorithm (e.g., H. A. Zebker, 2017; Zheng & Zebker, 2017). Because Sentinel-1 satel-
 190 lites have precise orbit controls, the spatial baselines of all interferogram pairs are much
 191 smaller than the InSAR critical baseline (Rosen et al., 2000). As a result, we did not ob-
 192 serve any noticeable spatial decorrelation artifacts, and our analysis is mainly focused
 193 on the mitigation of temporal decorrelation noise. Following the new workflow, we gener-
 194 ated all 6498 interferogram pairs without any spatial or temporal thresholds. To en-
 195 hance the spatial coherence of InSAR phase measurements, we selected PS pixels based
 196 on the cosine similarity method (Wang & Chen, 2022), performed a phase interpolation
 197 among PS pixels (J. Chen et al., 2015), and unwrapped InSAR phase measurements us-
 198 ing the Statistical-Cost, Network-flow Algorithm for Phase Unwrapping (SNAPHU) (C. Chen
 199 & Zebker, 2001) algorithm. We solved for the long-term deformation trend over the study
 200 period based on a linear deformation (constant velocity) model from interferograms with
 201 the phase unwrapping error $< 10,000$ radians. In a control SBAS experiment, we formed
 202 interferogram subsets with various temporal baseline thresholds (e.g., 12, 48, 360, and
 203 1000 days). For example, a 48-day interferogram subset contains all interferograms with
 204 ≤ 48 -day temporal baselines. For each small baseline subset, we unwrapped InSAR phase
 205 measurements using SNAPHU and solved for the cumulative LOS deformation over the
 206 study period based on the same linear deformation (constant velocity) model.

207 For the Texas case, we followed a similar processing strategy and processed 123 C-
 208 band Sentinel-1 images (path 107, frame 92). Using the new workflow, we generated all

209 7503 interferogram pairs without any spatial or temporal thresholds and improved In-
 210 SAR phase quality through a PS-interpolation. We solved for the cumulative LOS de-
 211 deformation over the study period based on a linear deformation model using a subset of
 212 interferograms with the total phase unwrapping error $< 100,000$ radians. In a control
 213 SBAS experiment, we chose temporal baseline thresholds of 12, 24, 48, 96, and 180 days
 214 to form small baseline interferogram subsets. For each small baseline subset, we unwrapped
 215 InSAR phase measurements and solved for the cumulative LOS deformation over the study
 216 period based on the same linear deformation model.

217 There are 25 permanent GPS stations with continuous records between 2017 and
 218 2021 over the Tulare Basin (Fig. S1, left). Because InSAR techniques only measure rel-
 219 ative deformation with respect to a reference pixel, we chose the GPS station P544 as
 220 the reference point to calibrate and used the remaining 24 GPS stations as controls to
 221 validate InSAR results. We projected the GPS daily East, North, and Up (ENU) time
 222 series (independently processed by the Nevada Geodetic Laboratory) to the radar LOS
 223 direction and estimated the average surface deformation rate in mm/year from both GPS
 224 and InSAR observations. We used the InSAR and GPS rate misfit, Δ_v to quantify the
 225 uncertainty in InSAR surface deformation solutions derived from different subsets. Sim-
 226 ilarly, we chose the GPS station TXFL as the reference point for the Texas case and used
 227 the remaining 5 stations as independent controls to validate InSAR results (Fig. S1, right).

228 4 Results and Discussion

229 4.1 The relationship between phase quality and temporal baselines

230 The Tulare Basin and Eagle Ford sites are covered with dense vegetation and the
 231 vegetation growth between radar acquisitions causes severe decorrelation, which appears
 232 random in space (e.g., Fig. 2 columns a and c). The InSAR phase measurement at a severely
 233 decorrelated radar pixel can be considered a random wrapped phase value between 0 and
 234 2π , and no longer contains spatially coherent phase information such as surface defor-
 235 mation signals or tropospheric noise. Unwrapping interferograms with severe decorre-
 236 lation artifacts is time-consuming and unreliable, and often introduces large phase un-
 237 wrapping errors that dominate in the final InSAR time series solutions. We emphasize
 238 that not all radar pixels decorrelate at the same rate. For example, roads, buildings, and
 239 rock outcrops can remain coherent over a much longer period of time than agricultural
 240 field pixels. Therefore, we identified phase measurements at relatively stable PS pixels
 241 and interpolated between PS pixels to improve InSAR spatial phase coherence (e.g., Fig.
 242 2 columns b and d) and reduced unwrapping time (Table S1).

243 An important finding of this study is that temporal baseline is not always a robust
 244 measure for selecting the interferogram subset (Fig. 2). For the Texas case, some recon-
 245 structed interferograms with longer temporal baselines (e.g., over 400 days) contain smaller
 246 phase unwrapping errors than those with shorter temporal baselines (e.g., 60 days). We
 247 found that interferograms formed from winter SAR scenes often have better phase co-
 248 herence than interferograms formed from summer SAR scenes. This is because after de-
 249 ciduous trees lose their leaves in the fall, radar signals reflected from tree trunks can main-
 250 tain coherence over a long period of time. Furthermore, some radar images contain large
 251 tropospheric noise anomalies due to heat waves or tropical storms (Staniewicz et al., 2020).
 252 Interferograms formed using these radar images tend to suffer from severe decorrelation
 253 noise regardless of temporal baselines. In summary, we identified a total of 2360 (out of
 254 7503) interferograms with phase unwrapping errors $< 100,000$ radians for the Texas case.
 255 Among these interferograms, there are 865 that span >200 days and 188 interferograms
 256 that span >1 year. For the California case, we identified a total of 527 (out of 6389) in-
 257 terferograms with phase unwrapping errors $< 10,000$ radians. Among those interfero-
 258 grams, 127 interferograms span >60 days and 7 span >90 days. We imposed a smaller
 259 total phase unwrapping error threshold for the California case because: (1) while dense

260 vegetation is only present over a portion of the Tulare Basin site covered with agricul-
 261 tural fields, it is present over the entire Eagle Ford site (Fig. S1). Therefore, the total
 262 phase unwrapping error is smaller in the Tulare Basin interferograms than in the Eagle
 263 Ford interferograms when similar decorrelation artifacts occur; and (2) the expected sub-
 264 sidence trend is much larger at the Tulare Basin site than the Eagle Ford site. Fewer in-
 265 terferograms are required to reduce tropospheric noise in order to reconstruct a larger
 266 deformation signal. In addition, interferograms with large deformation signals (e.g. Tu-
 267 lare Basin interferograms with long temporal baselines) may be prone to aliasing because
 268 the density of high-quality InSAR pixels is too low to capture the rapidly changing In-
 269 SAR fringes (Pepin & Zebker, 2024).

270 4.2 The Tulare Basin results

271 The Tulare Basin LOS deformation estimates derived from a subset of interfero-
 272 grams with small phase unwrapping errors show up to 150 mm/yr LOS deformation (Fig.
 273 3a) with a mean absolute error (MAE) of 3.4 mm/yr and a maximum absolute error of
 274 9.1 mm/yr based on independent GPS validation (Fig. 3g and Table S2). The observed
 275 deformation pattern is geographically consistent with recent InSAR studies (e.g., Farr,
 276 2018; Murray & Lohman, 2018; Ojha et al., 2019; Neely et al., 2021; Kang & Knight, 2023).
 277 For example, Neely et al. (2021) analyzed 263 Sentinel-1 interferograms (with tempo-
 278 ral baselines < 100 days) and observed up to ~ 270 mm/yr subsidence between April
 279 2015 and October 2017. The average velocity residual was 2.9 mm/yr based on indepen-
 280 dent GPS validation. They found that the subsidence rate changes throughout the year
 281 in response to water demand. Up to 345 mm/yr vertical subsidence (with an average ve-
 282 locity residual of 6.4 mm/yr) was observed during the dry period of October 2015 - Septem-
 283 ber 2016, while up to 177 mm/yr vertical subsidence (with an average velocity residual
 284 of 11.1 mm/yr) was observed during the wet period of October 2016 - September 2017.
 285 Ojha et al. (2019) and Kang and Knight (2023) reported similar error residuals but dif-
 286 ferent rate magnitudes, likely due to differences in the study period and InSAR process-
 287 ing methodologies.

288 To further illustrate how the InSAR processing strategy may influence SBAS so-
 289 lutions, Fig. 3b-f shows the LOS surface deformation rate estimates derived from dif-
 290 ferent small baseline subsets. The deformation solution derived from the 12-day inter-
 291 ferogram subset (denoted as "SBAS-12") shows an MAE of 13.9 mm/yr and a maximum
 292 absolute error of 29.2 mm/yr (Fig. 3g and Table S2). Given that we observed minimal
 293 decorrelation artifacts (thus minimal phase unwrapping errors) in 12-day interferograms,
 294 the errors in the SBAS-12 solution are primarily due to tropospheric noise. The SBAS-
 295 48 solution shows an MAE of 3.7 mm/yr and a maximum absolute error of 9.7 mm/yr,
 296 which is comparable to the deformation solution derived from the interferogram subset
 297 with small phase unwrapping errors. We again observed minimal decorrelation artifacts
 298 in the SBAS-48 interferogram subset, and tropospheric noise is the primary error source.
 299 In this case, interferograms with longer temporal baselines contain larger secular defor-
 300 mation signals than interferograms with shorter temporal baselines, while the tropospheric
 301 noise level among these interferograms is similar. As a result, the inclusion of interfer-
 302 ograms with longer temporal baselines can better reduce the residual tropospheric noise
 303 level in the SBAS deformation rate estimates (Supporting Information S1). However, the
 304 deformation solutions derived from a subset of interferograms with temporal baselines
 305 up to 180, 360, and 1000 days have an increasing MAE of 4.3, 5.2, and 11.5 mm/yr. This
 306 is because decorrelation artifacts are observed in interferograms with temporal baselines
 307 ~ 2 months and longer. As the temporal baseline threshold increases, more decorrelated
 308 InSAR phase observations are used in the SBAS inversion. In particular, most of the in-
 309 terferograms in the SBAS-1000 subset are completely decorrelated over the agricultural
 310 fields. As a result, fitting a linear deformation model to decorrelated InSAR observa-
 311 tions may yield a near-zero deformation rate estimate when the number of decorrelated ob-
 312 servations is sufficiently large. A systematic underestimation (up to 55.2 mm/yr) was

313 observed in the SBAS-1000 solution at all GPS stations where a non-trivial deformation
 314 signal is present (Fig. 3g and Table S2). We emphasize it is important to evaluate the
 315 accuracy of InSAR deformation estimates at GPS stations where non-trivial deformation
 316 is present. Because a large number of random decorrelated InSAR observations may
 317 yield near-zero deformation rate estimates, they often appear to be "consistent" with GPS
 318 observations at relatively stable locations. However, this does not mean decorrelated In-
 319 SAR measurements contain any information about the true deformation signals, and they
 320 should be excluded in the SBAS inversion.

321 4.3 The Eagle Ford region results

322 The Eagle Ford LOS deformation estimates derived from a subset of interferograms
 323 with small phase unwrapping error reveals a ~ 900 km² region of up to 11 cm of cumu-
 324 lative LOS deformation between February 2017 and December 2021 (Fig. 4a). The MAE
 325 at 5 GPS permanent stations is 2.7 mm/year and a maximum absolute error is 4.8 mm/year
 326 at TXCU (Fig. 4a and Table S3). The observed subsidence signal (Fig. 4a) aligns well
 327 with oil and gas production wells (The Railroad Commission of Texas, 2023). This re-
 328 gion experienced a ramp-up in oil and gas production around 2010. Approximately 20-
 329 25 million barrels of oil (bbl) and 100-120 million one thousand cubic feet (mcf) of gas
 330 were produced every month since 2014 (The Railroad Commission of Texas, 2023). Sim-
 331 ilarly, comparable volumes of subsurface water are co-produced with oil and gas. Ap-
 332 proximately 1246 million bbl of water from unconventional wells was produced from 2009-
 333 2016 in the Eagle Ford with 337, 291, and 206 million bbl of produced water each year
 334 for 2014, 2015, and 2016 respectively (Scanlon et al., 2019). Here, it is likely that the
 335 production of water, oil, and gas all contribute to the observed land subsidence (Fig. S2).

336 In contrast, the LOS surface deformation rate estimates derived from different small
 337 baseline subsets failed to detect this large deformation signal (Fig. 4b-f). The SBAS so-
 338 lution derived from the 12-day interferogram subset (Fig. 4b) has an MAE of 5.5 mm/yr
 339 and a maximum absolute error of 16 mm/yr. Given that we observed minimal decorre-
 340 lation artifacts in the 12-day interferograms (e.g., Fig. S3a and g), the residuals are mostly
 341 due to tropospheric noise. We note that there are only five GPS validation stations over
 342 the Eagle Ford region. As a result, the GPS-InSAR misfit only represents the InSAR mea-
 343 surement accuracy at these five locations (Table S3), and InSAR noise residuals can be
 344 much larger over regions with visible tropospheric noise artifacts. Because the study site
 345 is densely vegetated, we observed decorrelation artifacts and associated phase unwrap-
 346 ping errors even in some 24-day interferograms (Fig. S3h). As a result, both tropospheric
 347 noise and decorrelation artifacts are present in the SBAS-24 solution, and decorrelation-
 348 related artifacts dominate in the SBAS-48, SBAS-96, and SBAS-180 solutions. While
 349 unwrapping errors often lead to a systematic underestimation of the true deformation
 350 rate (e.g., in the Tulare Basin case Fig. 3f), decorrelation signatures can sometimes be
 351 unpredictable. In the Eagle Ford case, very large phase unwrapping errors are present
 352 in a subset of interferograms, which produced unrealistic artifacts in the SBAS-48, SBAS-
 353 96, and SBAS-180 solutions. We emphasize that it is important to employ a phase re-
 354 construction technique to enhance phase quality prior to the surface deformation anal-
 355 ysis over densely vegetated areas such as the Eagle Ford region. However, some long tem-
 356 poral baseline interferograms are reconstructed successfully, while some short temporal
 357 baseline interferograms fail to be reconstructed (Fig. 2). Therefore, selecting interfer-
 358 ograms based on an unwrapping error threshold is more robust than a temporal base-
 359 line threshold over regions with large tropospheric noise and severe decorrelation arti-
 360 facts.

361 While there are numerous InSAR surface deformation studies over the less vege-
 362 tated Permian Basin in West Texas (Kim & Lu, 2018; Staniewicz et al., 2020; Zhai et
 363 al., 2021; Hennings et al., 2021; Pepin et al., 2022), our study is the first that observes
 364 a large subsidence feature with spatially dense information over the Eagle Ford region

365 in Central Texas. Surface deformation can be used to derive subsurface stress and pore
 366 pressure changes related to oil and gas injection and extraction (e.g., Yang et al., 2015;
 367 Vasco et al., 2016; Shirzaei et al., 2019; Deng et al., 2020). These changes in the sub-
 368 surface can eventually result in fault slip and trigger earthquakes (Segall, 1989). For ex-
 369 ample, Frohlich and Brunt (2013) reported 62 earthquakes in the Eagle Ford region from
 370 2009-2011, highlighted by a M_w 4.8 earthquake in October 2011 in Fashing, TX. They
 371 found that most of the seismicity followed fluid extraction, not injection. Recently, the
 372 Eagle Ford region has experienced a noticeable increase in seismic activity, and there were
 373 165, 341, 336, 349 earthquakes recorded in 2017-2018, 2019-2020, 2021-2022, 2023-March
 374 13, 2024, respectively (Fig. 4a) (TexNet, 2024). In particular, two earthquakes (M_L 4.3
 375 and M_L 4.7) occurred on February 17, 2024 near Falls City, which were felt by many San
 376 Antonio and Austin residents. The increase in magnitude and frequency of these large
 377 seismic events requires further scientific investigation, and InSAR data can play an im-
 378 portant role in these future induced seismicity studies.

379 5 Conclusion

380 In this study, we found that selecting an interferogram subset based on phase qual-
 381 ity rather than temporal baseline leads to better mitigation of decorrelation and tropo-
 382 spheric noise. In the Tulare Basin case, our InSAR processing strategy generated a de-
 383 formation solution comparable to the SBAS solution when the optimal temporal base-
 384 line threshold was employed. In the Eagle Ford case, our processing strategy revealed
 385 a large subsidence signature associated with oil and gas operations that is otherwise un-
 386 detectable due to the presence of large tropospheric noise and severe decorrelation ar-
 387 tifacts. Our workflow is easy to implement, which can extend the use of the SBAS al-
 388 gorithm over humid and densely vegetated terrain that is challenging for InSAR stud-
 389 ies.

390 6 Open Research

391 Sentinel-1 SAR imagery over the Tulare Basin, CA (path 137, frame 114) and Ea-
 392 gle Ford region, TX (path 107, frame 92) can be queried and downloaded from the Alaska
 393 Satellite Facility at <https://search.asf.alaska.edu>. Interferograms with comparable qual-
 394 ity can be produced using InSAR processing packages such as the InSAR Scientific Com-
 395 puting Environment 3 (ISCE3) (Rosen et al., 2018), GMTSAR (Sandwell et al., 2011),
 396 or GAMMA (Wegmüller et al., 2016). GPS data were processed by the Nevada Geode-
 397 tic Laboratory and downloaded at <http://geodesy.unr.edu/NGLStationPages/GlobalStationList>
 398 (Blewitt et al., 2018). A list of available GPS stations over the Tulare Basin and the Ea-
 399 gle Ford region can be found in the Supporting Information.

400 Acknowledgments

401 This research was funded by the NASA Earth Surface and Interior Program grant num-
 402 bers 80NSSC18K0467 and 80NSSC22K0412.

403 References

- 404 Agram, P. (2010, 01). Persistent scatterer interferometry in natural terrain.
 405 Amelung, F., Galloway, D. L., Bell, J. W., Zebker, H. A., & Laczniak, R. J. (1999,
 406 06). Sensing the ups and downs of Las Vegas: InSAR reveals structural con-
 407 trol of land subsidence and aquifer-system deformation. *Geology*, *27*(6), 483-
 408 486. Retrieved from [https://doi.org/10.1130/0091-7613\(1999\)027<0483:](https://doi.org/10.1130/0091-7613(1999)027<0483:STUADO>2.3.CO;2)
 409 [STUADO>2.3.CO;2](https://doi.org/10.1130/0091-7613(1999)027<0483:STUADO>2.3.CO;2) doi: 10.1130/0091-7613(1999)027<0483:STUADO>2.3.CO;
 410 2
 411 Ansari, H., De Zan, F., & Bamler, R. (2018). Efficient phase estimation for interfer-

- ogram stacks. *IEEE Transactions on Geoscience and Remote Sensing*, 56(7), 4109-4125. doi: 10.1109/TGRS.2018.2826045
- 412
413
- Ansari, H., De Zan, F., & Parizzi, A. (2021). Study of systematic bias in measuring surface deformation with SAR interferometry. *IEEE Transactions on Geoscience and Remote Sensing*, 59(2), 1285-1301. doi: 10.1109/TGRS.2020.3003421
- 414
415
416
417
- Bekaert, D., Hooper, A., & Wright, T. J. (2015a). A spatially variable power law tropospheric correction technique for InSAR data. *Journal of Geophysical Research: Solid Earth*, 120(2), 1345-1356. Retrieved from <https://agupubs.onlinelibrary.wiley.com/doi/abs/10.1002/2014JB011558> doi: <https://doi.org/10.1002/2014JB011558>
- 418
419
420
421
422
- Bekaert, D., Walters, R., Wright, T., Hooper, A., & Parker, D. (2015b, 09). Statistical comparison of InSAR tropospheric correction techniques. *Remote Sensing of Environment*, 170, 40-47. doi: 10.1016/j.rse.2015.08.035
- 423
424
425
- Bell, J., Amelung, F., Ferretti, A., Bianchi, M., & Novali, F. (2008, 02). Permanent scatterer InSAR reveals seasonal and long-term aquifer-system response to groundwater pumping and artificial recharge. *Water Resources Research*, 44. doi: 10.1029/2007WR006152
- 426
427
428
429
- Berardino, P., Fornaro, G., Lanari, R., & Sansosti, E. (2002). A new algorithm for surface deformation monitoring based on small baseline differential SAR interferograms. *IEEE Transactions on Geoscience and Remote Sensing*, 40(11), 2375-2383. doi: 10.1109/TGRS.2002.803792
- 430
431
432
433
- Bevis, M., Businger, S., Herring, T. A., Rocken, C., Anthes, R. A., & Ware, R. H. (1992). GPS meteorology: Remote sensing of atmospheric water vapor using the global positioning system. *Journal of Geophysical Research: Atmospheres*, 97(D14), 15787-15801. Retrieved from <https://agupubs.onlinelibrary.wiley.com/doi/abs/10.1029/92JD01517> doi: <https://doi.org/10.1029/92JD01517>
- 434
435
436
437
438
439
- Blewitt, G., Hammond, W. C., & Kreemer, C. (2018). Harnessing the GPS data explosion for interdisciplinary science. *EOS*, 99. doi: <https://doi.org/10.1029/2018EO104623>
- 440
441
442
- Chaussard, E., Bürgmann, R., Shirzaei, M., Fielding, E. J., & Baker, B. (2014). Predictability of hydraulic head changes and characterization of aquifer-system and fault properties from InSAR-derived ground deformation. *Journal of Geophysical Research: Solid Earth*, 119(8), 6572-6590. Retrieved from <https://agupubs.onlinelibrary.wiley.com/doi/abs/10.1002/2014JB011266> doi: <https://doi.org/10.1002/2014JB011266>
- 443
444
445
446
447
448
- Chen, C., & Zebker, H. (2001, 03). Two-dimensional phase unwrapping with use of statistical models for cost functions in nonlinear optimization. *Journal of the Optical Society of America. A, Optics, image science, and vision*, 18, 338-51. doi: 10.1364/JOSAA.18.000338
- 449
450
451
452
- Chen, J., Zebker, H. A., & Knight, R. (2015). A persistent scatterer interpolation for retrieving accurate ground deformation over InSAR-decorrelated agricultural fields. *Geophysical Research Letters*, 42(21), 9294-9301. Retrieved from <https://agupubs.onlinelibrary.wiley.com/doi/abs/10.1002/2015GL065031> doi: <https://doi.org/10.1002/2015GL065031>
- 453
454
455
456
457
- Deng, F., Dixon, T. H., & Xie, S. (2020). Surface deformation and induced seismicity due to fluid injection and oil and gas extraction in Western Texas. *Journal of Geophysical Research: Solid Earth*, 125(5), e2019JB018962. Retrieved from <https://agupubs.onlinelibrary.wiley.com/doi/abs/10.1029/2019JB018962> (e2019JB018962 2019JB018962) doi: <https://doi.org/10.1029/2019JB018962>
- 458
459
460
461
462
463
- Doin, M., Lasserre, C., Peltzer, G., Cavalié, O., & Doubre, C. (2009). Corrections of stratified tropospheric delays in SAR interferometry: Validation with global atmospheric models. *Journal of Applied Geophysics*, 69(1), 35-50.
- 464
465
466

- Retrieved from <https://www.sciencedirect.com/science/article/pii/S0926985109000603> (Advances in SAR Interferometry from the 2007 Fringe Workshop) doi: <https://doi.org/10.1016/j.jappgeo.2009.03.010>
- Emardson, T., Simons, M., & Webb, F. (2003, 05). Neural atmospheric delay in interferometric Synthetic Aperture Radar applications: statistical description and mitigation. *Journal of Geophysical Research*, *108*. doi: 10.1029/2002JB001781
- Farr, T. G. (2018). InSAR measurements of subsidence and rebound in California. In *IGARSS 2018 - 2018 IEEE International Geoscience and Remote Sensing Symposium* (p. 8401-8403). IEEE.
- Farr, T. G., & Liu, Z. (2015). Monitoring subsidence associated with ground water dynamics in the Central Valley of California using interferometric radar. *Geophysical Monograph*, *206*, 397-406.
- Fattahi, H., & Amelung, F. (2013). DEM error correction in InSAR time series. *IEEE Transactions on Geoscience and Remote Sensing*, *51*(7), 4249-4259. doi: 10.1109/TGRS.2012.2227761
- Fattahi, H., Simons, M., & Agram, P. (2017). InSAR time-series estimation of the ionospheric phase delay: An extension of the split range-spectrum technique. *IEEE Transactions on Geoscience and Remote Sensing*, *55*(10), 5984-5996. doi: 10.1109/TGRS.2017.2718566
- Faunt, C. C., Sneed, M., Traum, J., & Brandt, J. T. (2016). Water availability and land subsidence in the Central Valley, California, USA. *Hydrogeology journal*, *24*(3), 675-684.
- Ferretti, A., Fumagalli, A., Novali, F., Prati, C., Rocca, F., & Rucci, A. (2011). A new algorithm for processing interferometric data-stacks: SqueeSAR. *IEEE Transactions on Geoscience and Remote Sensing*, *49*(9), 3460-3470. doi: 10.1109/TGRS.2011.2124465
- Ferretti, A., Prati, C., & Rocca, F. (2000). Nonlinear subsidence rate estimation using permanent scatterers in differential SAR interferometry. *IEEE Transactions on Geoscience and Remote Sensing*, *38*(5), 2202-2212. doi: 10.1109/36.868878
- Fialko, Y., Sandwell, D., Agnew, D., Simons, M., Shearer, P., & Minster, B. (2002). Deformation on nearby faults induced by the 1999 Hector Mine earthquake. *Science*, *297*(5588), 1858-1862. Retrieved from <https://www.science.org/doi/abs/10.1126/science.1074671> doi: 10.1126/science.1074671
- Fielding, E., Sangha, S., Bekaert, D., Samsonov, S., & Chang, J. (2017, 07). Surface deformation of North-Central Oklahoma related to the 2016 Mw 5.8 Pawnee earthquake from SAR interferometry time series. *Seismological Research Letters*, *88*, 971-982. doi: 10.1785/0220170010
- Fornaro, G., Verde, S., Reale, D., & Pauciuillo, A. (2015). CAESAR: An approach based on covariance matrix decomposition to improve multibaseline-multitemporal interferometric SAR processing. *IEEE Transactions on Geoscience and Remote Sensing*, *53*(4), 2050-2065. doi: 10.1109/TGRS.2014.2352853
- Frohlich, C., & Brunt, M. (2013). Two-year survey of earthquakes and injection/production wells in the Eagle Ford Shale, Texas, prior to the MW4.8 20 October 2011 earthquake. *Earth and Planetary Science Letters*, *379*, 56-63. Retrieved from <https://www.sciencedirect.com/science/article/pii/S0012821X13004007> doi: <https://doi.org/10.1016/j.epsl.2013.07.025>
- Galloway, D. L., Jones, D. R. D. R., & Ingebritsen, S. E. (1999). *Land subsidence in the United States / edited by Devin Galloway, David R. Jones, S.E. Ingebritsen*. Reston, VA: U.S. Geological Survey.
- Guarnieri, A. M., & Tebaldini, S. (2008). On the exploitation of target statistics for SAR interferometry applications. *IEEE Transactions on Geoscience and Remote Sensing*, *46*(11), 3436-3443. doi: 10.1109/TGRS.2008.2001756

- 522 Hanssen, R. (2001). *Radar interferometry: Data interpretation and error analysis*.
523 Springer.
- 524 Hennings, P., Dvory, N., Horne, E., Li, P., Savvaïdis, A., & Zoback, M. (2021,
525 08). Stability of the Fault Systems That Host-Induced Earthquakes in the
526 Delaware Basin of West Texas and Southeast New Mexico. *The Seismic*
527 *Record*, 1(2), 96-106. Retrieved from <https://doi.org/10.1785/0320210020>
528 doi: 10.1785/0320210020
- 529 Hoffmann, J., Zebker, H., Galloway, D., & Amelung, F. (2001, 06). Seasonal subsi-
530 dence and rebound in Las Vegas Valley, Nevada, observed by Synthetic Aper-
531 ture Radar Interferometry. *Water Resources Research*, 37, 1551-1566. doi:
532 10.1029/2000WR900404
- 533 Hooper, A., Zebker, H., Segall, P., & Kampes, B. (2004). A new method for
534 measuring deformation on volcanoes and other natural terrains using In-
535 SAR persistent scatterers. *Geophysical Research Letters*, 31(23). Retrieved
536 from [https://agupubs.onlinelibrary.wiley.com/doi/abs/10.1029/](https://agupubs.onlinelibrary.wiley.com/doi/abs/10.1029/2004GL021737)
537 [2004GL021737](https://doi.org/10.1029/2004GL021737) doi: <https://doi.org/10.1029/2004GL021737>
- 538 Huang, S. A., & Zebker, H. A. (2022). InSAR time-series analysis with a non-
539 Gaussian detector for persistent scatterers. *IEEE Journal of Selected Topics*
540 *in Applied Earth Observations and Remote Sensing*, 15, 9208-9225. doi:
541 10.1109/JSTARS.2022.3216964
- 542 Jolivet, R., Grandin, R., Lasserre, C., Doin, M.-P., & Peltzer, G. (2011). Systematic
543 InSAR tropospheric phase delay corrections from global meteorological reanal-
544 ysis data. *Geophysical Research Letters*, 38(17). Retrieved from [https://](https://agupubs.onlinelibrary.wiley.com/doi/abs/10.1029/2011GL048757)
545 [agupubs.onlinelibrary.wiley.com/doi/abs/10.1029/2011GL048757](https://doi.org/10.1029/2011GL048757) doi:
546 <https://doi.org/10.1029/2011GL048757>
- 547 Jónsson, S., Amelung, F., Zebker, H., & Segall, P. (2000). Widespread uplift and
548 'trapdoor' faulting on galápagos volcanoes observed with radar interferometry.
549 *Nature (London)*, 407(6807), 993-996.
- 550 Kang, S., & Knight, R. (2023). Isolating the poroelastic response of the groundwa-
551 ter system in InSAR data from the Central Valley of California. *Geophys-*
552 *ical Research Letters*, 50(9), e2023GL103222. Retrieved from [https://](https://agupubs.onlinelibrary.wiley.com/doi/abs/10.1029/2023GL103222)
553 [agupubs.onlinelibrary.wiley.com/doi/abs/10.1029/2023GL103222](https://doi.org/10.1029/2023GL103222)
554 (e2023GL103222 2023GL103222) doi: <https://doi.org/10.1029/2023GL103222>
- 555 Kim, J.-W., & Lu, Z. (2018, 03). Association between localized geohazards in
556 West Texas and human activities, recognized by Sentinel-1A/B satellite radar
557 imagery. *Scientific Reports*, 8. doi: 10.1038/s41598-018-23143-6
- 558 Li, Z., Fielding, E. J., Cross, P., & Preusker, R. (2009). Advanced InSAR at-
559 mospheric correction: MERIS/MODIS combination and stacked water
560 vapour models. *International Journal of Remote Sensing*, 30(13), 3343-
561 3363. Retrieved from <https://doi.org/10.1080/01431160802562172> doi:
562 10.1080/01431160802562172
- 563 Lundgren, P., Poland, M., Miklius, A., Orr, T., Yun, S.-H., Fielding, E., ...
564 Owen, S. (2013). Evolution of dike opening during the march 2011
565 kamoamoā fissure eruption, kilauea volcano, hawai'i. *Journal of Geophys-*
566 *ical Research: Solid Earth*, 118(3), 897-914. Retrieved from [https://](https://agupubs.onlinelibrary.wiley.com/doi/abs/10.1002/jgrb.50108)
567 [agupubs.onlinelibrary.wiley.com/doi/abs/10.1002/jgrb.50108](https://doi.org/10.1002/jgrb.50108) doi:
568 <https://doi.org/10.1002/jgrb.50108>
- 569 McKeighan, C., Hennings, P., Horne, E. A., Smye, K., & Morris, A. (2022, 10).
570 Understanding Anthropogenic Fault Rupture in the Eagle Ford Region, South-
571 Central Texas. *Bulletin of the Seismological Society of America*, 112(6),
572 2870-2889. Retrieved from <https://doi.org/10.1785/0120220074> doi:
573 10.1785/0120220074
- 574 Mirzaee, S., Amelung, F., & Fattahi, H. (2023). Non-linear phase linking using
575 joined distributed and persistent scatterers. *Computers Geosciences*, 171,
576 105291. Retrieved from <https://www.sciencedirect.com/science/article/>

- 577 pii/S0098300422002400 doi: <https://doi.org/10.1016/j.cageo.2022.105291>
- 578 Murray, K. D., & Lohman, R. B. (2018). Short-lived pause in Central California
579 subsidence after heavy winter precipitation of 2017. *Science Advances*, 4(8),
580 eaar8144. Retrieved from [https://www.science.org/doi/abs/10.1126/](https://www.science.org/doi/abs/10.1126/sciadv.aar8144)
581 [sciadv.aar8144](https://www.science.org/doi/abs/10.1126/sciadv.aar8144) doi: 10.1126/sciadv.aar8144
- 582 Neely, W. R., Borsa, A. A., Burney, J. A., Levy, M. C., Silverii, F., & Sneed, M.
583 (2021). Characterization of groundwater recharge and flow in California's San
584 Joaquin Valley from InSAR-observed surface deformation. *Water resources*
585 *research*, 57(4), e2020WR028451-n/a.
- 586 Ojha, C., Shirzaei, M., Werth, S., Argus, D. F., & Farr, T. G. (2018). Sus-
587 tained groundwater loss in California's Central Valley exacerbated by intense
588 drought periods. *Water Resources Research*, 54(7), 4449-4460. Retrieved
589 from [https://agupubs.onlinelibrary.wiley.com/doi/abs/10.1029/](https://agupubs.onlinelibrary.wiley.com/doi/abs/10.1029/2017WR022250)
590 [2017WR022250](https://agupubs.onlinelibrary.wiley.com/doi/abs/10.1029/2017WR022250) doi: <https://doi.org/10.1029/2017WR022250>
- 591 Ojha, C., Werth, S., & Shirzaei, M. (2019). Groundwater loss and aquifer system
592 compaction in San Joaquin Valley during 2012–2015 drought. *Journal of Geo-*
593 *physical Research: Solid Earth*, 124(3), 3127-3143. Retrieved from [https://](https://agupubs.onlinelibrary.wiley.com/doi/abs/10.1029/2018JB016083)
594 agupubs.onlinelibrary.wiley.com/doi/abs/10.1029/2018JB016083 doi:
595 <https://doi.org/10.1029/2018JB016083>
- 596 Pepin, K., Ellsworth, W., Sheng, Y., & Zebker, H. (2022, 02). Shallow aseismic slip
597 in the Delaware Basin determined by Sentinel-1 InSAR. *Journal of Geophysical*
598 *Research: Solid Earth*, 127. doi: 10.1029/2021JB023157
- 599 Pepin, K., & Zebker, H. (2024). Aliasing in InSAR 2d phase unwrapping and time
600 series. *IEEE Transactions on Geoscience and Remote Sensing*, 1-1. doi: 10
601 .1109/TGRS.2024.3359482
- 602 Poland, J. F. J. F. (1975). *Land subsidence, in the San Joaquin Valley, California,*
603 *as of 1972 / by J. F. Poland [and three others]; prepared in cooperation with*
604 *the California Department of Water Resources.* Washington: United States
605 Department of the Interior, Geological Survey.
- 606 Pritchard, M., & Simons, M. (2002, 08). A satellite geodetic survey of large scale de-
607 formation of volcanic centers in the Central Andes. *Nature*, 418, 167-71. doi:
608 10.1038/nature00872
- 609 Rosen, P., Gurrola, E. M., Agram, P., Cohen, J., Lavalley, M., Riel, B. V., ... Buck-
610 ley, S. M. (2018). The insar scientific computing environment 3.0: A flexible
611 framework for nisar operational and user-led science processing. In *Igarss 2018*
612 *- 2018 ieee international geoscience and remote sensing symposium* (p. 4897-
613 4900). doi: 10.1109/IGARSS.2018.8517504
- 614 Rosen, P., Hensley, S., Joughin, I., Li, F., Madsen, S., Rodriguez, E., & Goldstein,
615 R. (2000, 04). Synthetic aperture radar interferometry. *Proceedings of the*
616 *IEEE*, 88, 333 - 382. doi: 10.1109/5.838084
- 617 Sandwell, D., Mellors, R., Tong, X., Wei, M., & Wessel, P. (2011). Gmtsar: An insar
618 processing system based on generic mapping tools.
- 619 Scanlon, B., Ikonnikova, S., Qian, Y., & Reedy, R. (2020, 02). Will water issues con-
620 strain oil and gas production in the U.S.? *Environmental Science Technology*,
621 54, 3510–3519. doi: 10.1021/acs.est.9b06390
- 622 Scanlon, B., Weingarten, M., Murray, K., & Reedy, R. (2019). Managing basin-scale
623 fluid budgets to reduce injection-induced seismicity from the recent u.s. shale
624 oil revolution. *Seismological research letters*, 90(1), 171-182.
- 625 Schmidt, D., & Burgmann, R. (2003, 09). Time-dependent land uplift and sub-
626 sidence in the Santa Clara valley, California, from a large interferometric
627 synthetic aperture radar data set. *Journal of Geophysical Research*, 108. doi:
628 10.1029/2002JB002267
- 629 Segall, P. (1989). Earthquakes triggered by fluid extraction. *Geology*, 17(10), 942-
630 946. Retrieved from [https://doi.org/10.1130/0091-7613\(1989\)017<0942:](https://doi.org/10.1130/0091-7613(1989)017<0942:ETBFE>2.3.CO;2)
631 [ETBFE>2.3.CO;2](https://doi.org/10.1130/0091-7613(1989)017<0942:ETBFE>2.3.CO;2) doi: 10.1130/0091-7613(1989)017<0942:ETBFE>2.3.CO;2

- 632 Shirzaei, M., & Bürgmann, R. (2013). Time-dependent model of creep on the
633 Hayward fault from joint inversion of 18 years of InSAR and surface creep
634 data. *Journal of Geophysical Research: Solid Earth*, *118*(4), 1733-1746.
635 Retrieved from [https://agupubs.onlinelibrary.wiley.com/doi/abs/](https://agupubs.onlinelibrary.wiley.com/doi/abs/10.1002/jgrb.50149)
636 [10.1002/jgrb.50149](https://doi.org/10.1002/jgrb.50149) doi: <https://doi.org/10.1002/jgrb.50149>
- 637 Shirzaei, M., Manga, M., & Zhai, G. (2019). Hydraulic properties of injection for-
638 mations constrained by surface deformation. *Earth and Planetary Science*
639 *Letters*, *515*, 125-134. Retrieved from [https://www.sciencedirect.com/](https://www.sciencedirect.com/science/article/pii/S0012821X19301736)
640 [science/article/pii/S0012821X19301736](https://www.sciencedirect.com/science/article/pii/S0012821X19301736) doi: [https://doi.org/10.1016/](https://doi.org/10.1016/j.epsl.2019.03.025)
641 [j.epsl.2019.03.025](https://doi.org/10.1016/j.epsl.2019.03.025)
- 642 Smith, R. G., Knight, R., Chen, J., Reeves, J. A., Zebker, H. A., Farr, T., & Liu, Z.
643 (2017). Estimating the permanent loss of groundwater storage in the southern
644 San Joaquin Valley, California. *Water Resources Research*, *53*(3), 2133-2148.
645 Retrieved from [https://agupubs.onlinelibrary.wiley.com/doi/abs/](https://agupubs.onlinelibrary.wiley.com/doi/abs/10.1002/2016WR019861)
646 [10.1002/2016WR019861](https://doi.org/10.1002/2016WR019861) doi: <https://doi.org/10.1002/2016WR019861>
- 647 Staniewicz, S., Chen, J., Lee, H., Olson, J., Savvaidis, A., Reedy, R., ... Hen-
648 nings, P. (2020). InSAR reveals complex surface deformation patterns
649 over an 80,000km² oil-producing region in the Permian Basin. *Geophysi-
650 cal Research Letters*, *47*(21), e2020GL090151. Retrieved from [https://](https://agupubs.onlinelibrary.wiley.com/doi/abs/10.1029/2020GL090151)
651 agupubs.onlinelibrary.wiley.com/doi/abs/10.1029/2020GL090151
652 ([e2020GL090151 10.1029/2020GL090151](https://doi.org/10.1029/2020GL090151)) doi: [https://doi.org/10.1029/](https://doi.org/10.1029/2020GL090151)
653 [2020GL090151](https://doi.org/10.1029/2020GL090151)
- 654 TexNet. (2024). *TexNet High Resolution Earthquake Catalog: Bureau for Eco-
655 nomic Geology at University of Texas at Austin*. Retrieved 2024-03-28, from
656 <https://doi.org/10.15781/76hj-ed46>
- 657 The Railroad Commission of Texas. (2023). *Eagle Ford Shale*. Retrieved 2024-03-
658 28, from [https://www.rrc.texas.gov/oil-and-gas/major-oil-and-gas](https://www.rrc.texas.gov/oil-and-gas/major-oil-and-gas-formations/eagle-ford-shale/)
659 [-formations/eagle-ford-shale/](https://www.rrc.texas.gov/oil-and-gas/major-oil-and-gas-formations/eagle-ford-shale/)
- 660 Tymofyeyeva, E., & Fialko, Y. (2015). Mitigation of atmospheric phase delays
661 in InSAR data, with application to the eastern California shear zone. *Jour-
662 nal of Geophysical Research: Solid Earth*, *120*(8), 5952-5963. Retrieved
663 from [https://agupubs.onlinelibrary.wiley.com/doi/abs/10.1002/](https://agupubs.onlinelibrary.wiley.com/doi/abs/10.1002/2015JB011886)
664 [2015JB011886](https://doi.org/10.1002/2015JB011886) doi: <https://doi.org/10.1002/2015JB011886>
- 665 Vasco, D., Harness, P., Pride, S., & Hoversten, M. (2016, 12). Estimating fluid-
666 induced stress change from observed deformation. *Geophysical Journal Inter-
667 national*, *208*(3), 1623-1642. Retrieved from [https://doi.org/10.1093/gji/](https://doi.org/10.1093/gji/ggw472)
668 [ggw472](https://doi.org/10.1093/gji/ggw472) doi: [10.1093/gji/ggw472](https://doi.org/10.1093/gji/ggw472)
- 669 Wadge, G., Webley, P. W., James, I. N., Bingley, R., Dodson, A., Waugh, S.,
670 ... Clarke, P. J. (2002). Atmospheric models, GPS and InSAR mea-
671 surements of the tropospheric water vapour field over Mount Etna. *Geo-
672 physical Research Letters*, *29*(19), 11-1-11-4. Retrieved from [https://](https://agupubs.onlinelibrary.wiley.com/doi/abs/10.1029/2002GL015159)
673 agupubs.onlinelibrary.wiley.com/doi/abs/10.1029/2002GL015159 doi:
674 <https://doi.org/10.1029/2002GL015159>
- 675 Wang, K., & Chen, J. (2022). Accurate persistent scatterer identification based on
676 phase similarity of radar pixels. *IEEE Transactions on Geoscience and Remote*
677 *Sensing*, *60*, 1-13. doi: [10.1109/TGRS.2022.3210868](https://doi.org/10.1109/TGRS.2022.3210868)
- 678 Wegmüller, U., Werner, C., Strozzi, T., Wiesmann, A., Frey, O., & Santoro, M.
679 (2016). Sentinel-1 support in the gamma software. *Procedia Computer Sci-
680 ence*, *100*, 1305-1312. Retrieved from [https://www.sciencedirect.com/](https://www.sciencedirect.com/science/article/pii/S1877050916324152)
681 [science/article/pii/S1877050916324152](https://www.sciencedirect.com/science/article/pii/S1877050916324152) (International Conference
682 on ENTERprise Information Systems/International Conference on Project
683 MANagement/International Conference on Health and Social Care Informa-
684 tion Systems and Technologies, CENTERIS/ProjMAN / HCist 2016) doi:
685 <https://doi.org/10.1016/j.procs.2016.09.246>
- 686 Wright, T. J., Parsons, B., England, P. C., & Fielding, E. J. (2004). InSAR observa-

- 687 tions of low slip rates on the major faults of western tibet. *Science*, *305*(5681),
688 236-239. Retrieved from [https://www.science.org/doi/abs/10.1126/](https://www.science.org/doi/abs/10.1126/science.1096388)
689 [science.1096388](https://www.science.org/doi/abs/10.1126/science.1096388) doi: 10.1126/science.1096388
- 690 Xu, X., Sandwell, D. T., Klein, E., & Bock, Y. (2021). Integrated Sentinel-1 In-
691 SAR and GNSS time-series along the San Andreas fault system. *Journal*
692 *of Geophysical Research: Solid Earth*, *126*(11), e2021JB022579. Retrieved
693 from [https://agupubs.onlinelibrary.wiley.com/doi/abs/10.1029/](https://agupubs.onlinelibrary.wiley.com/doi/abs/10.1029/2021JB022579)
694 [2021JB022579](https://agupubs.onlinelibrary.wiley.com/doi/abs/10.1029/2021JB022579) (e2021JB022579 2021JB022579) doi: [https://doi.org/10.1029/](https://doi.org/10.1029/2021JB022579)
695 [2021JB022579](https://doi.org/10.1029/2021JB022579)
- 696 Yang, Q., Zhao, W., Dixon, T., Amelung, F., Han, W., & Li, P. (2015, October 1).
697 InSAR monitoring of ground deformation due to CO2 injection at an en-
698 hanced oil recovery site, West Texas. *International Journal of Greenhouse*
699 *Gas Control*, *41*, 20–28. (Publisher Copyright: © 2015 Elsevier Ltd.) doi:
700 [10.1016/j.ijggc.2015.06.016](https://doi.org/10.1016/j.ijggc.2015.06.016)
- 701 Yu, C., Penna, N. T., & Li, Z. (2017). Generation of real-time mode high-
702 resolution water vapor fields from GPS observations. *Journal of Geophys-*
703 *ical Research: Atmospheres*, *122*(3), 2008-2025. Retrieved from [https://](https://agupubs.onlinelibrary.wiley.com/doi/abs/10.1002/2016JD025753)
704 agupubs.onlinelibrary.wiley.com/doi/abs/10.1002/2016JD025753 doi:
705 <https://doi.org/10.1002/2016JD025753>
- 706 Zebker, H. A. (2017). User-friendly insar data products: Fast and simple timeseries
707 processing. *IEEE Geoscience and Remote Sensing Letters*, *14*, 2122-2126.
- 708 Zebker, H. A., Rosen, P. A., & Hensley, S. (1997). Atmospheric effects in in-
709 terferometric synthetic aperture radar surface deformation and topographic
710 maps. *Journal of Geophysical Research: Solid Earth*, *102*(B4), 7547-7563.
711 Retrieved from [https://agupubs.onlinelibrary.wiley.com/doi/abs/](https://agupubs.onlinelibrary.wiley.com/doi/abs/10.1029/96JB03804)
712 [10.1029/96JB03804](https://agupubs.onlinelibrary.wiley.com/doi/abs/10.1029/96JB03804) doi: <https://doi.org/10.1029/96JB03804>
- 713 Zebker, H. A., & Villasenor, J. (1992). Decorrelation in interferometric radar echoes.
714 *IEEE Transactions on Geoscience and Remote Sensing*, *30*(5), 950-959. doi:
715 [10.1109/36.175330](https://doi.org/10.1109/36.175330)
- 716 Zebker, M. S., Chen, J., & Hesse, M. A. (2023). Robust surface deformation and
717 tropospheric noise characterization from common-reference interferogram sub-
718 sets. *IEEE Transactions on Geoscience and Remote Sensing*, *61*, 1-14. doi:
719 [10.1109/TGRS.2023.3288019](https://doi.org/10.1109/TGRS.2023.3288019)
- 720 Zhai, G., Shirzaei, M., & Manga, M. (2021, 05). Widespread deep seismicity in the
721 Delaware Basin, Texas, is mainly driven by shallow wastewater injection. *Pro-*
722 *ceedings of the National Academy of Sciences*, *118*, e2102338118. doi: 10.1073/
723 [pnas.2102338118](https://doi.org/10.1073/pnas.2102338118)
- 724 Zheng, Y., Fattahi, H., Agram, P., Simons, M., & Rosen, P. (2022). On closure
725 phase and systematic bias in multilooked SAR interferometry. *IEEE transac-*
726 *tions on geoscience and remote sensing*, *60*, 1-11.
- 727 Zheng, Y., Zebker, H., & Michaelides, R. (2021). A new decorrelation phase co-
728 variance model for noise reduction in unwrapped interferometric phase stacks.
729 *IEEE Transactions on Geoscience and Remote Sensing*, *59*(12), 10126-10135.
730 doi: 10.1109/TGRS.2021.3050087
- 731 Zheng, Y., & Zebker, H. A. (2017). Phase correction of single-look complex radar
732 images for user-friendly efficient interferogram formation. *IEEE Journal of*
733 *Selected Topics in Applied Earth Observations and Remote Sensing*, *10*, 2694-
734 2701.

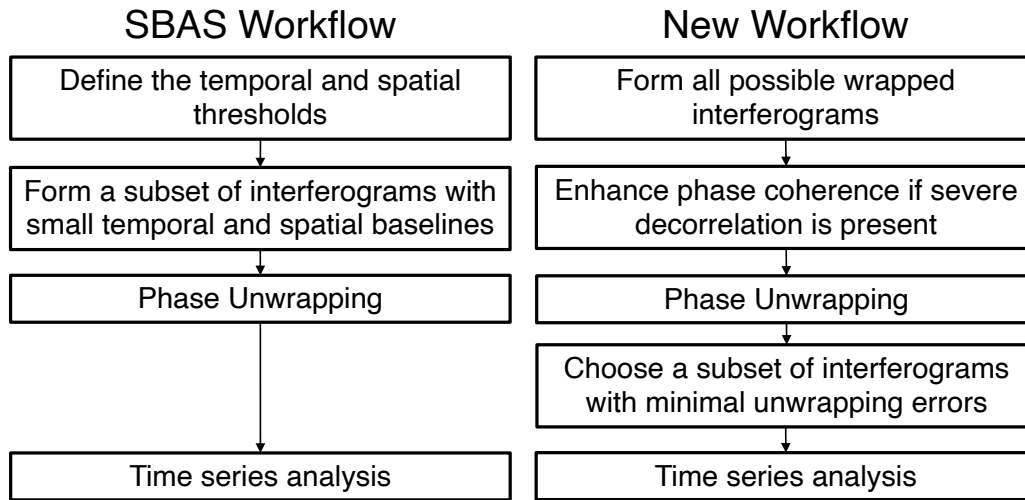


Figure 1. (Left) SBAS InSAR time series analysis workflow. (Right) The new workflow that first mitigates decorrelation noise through InSAR phase reconstruction, then selects the an interferogram subset based on the quality of InSAR phase measurements for time series analysis.

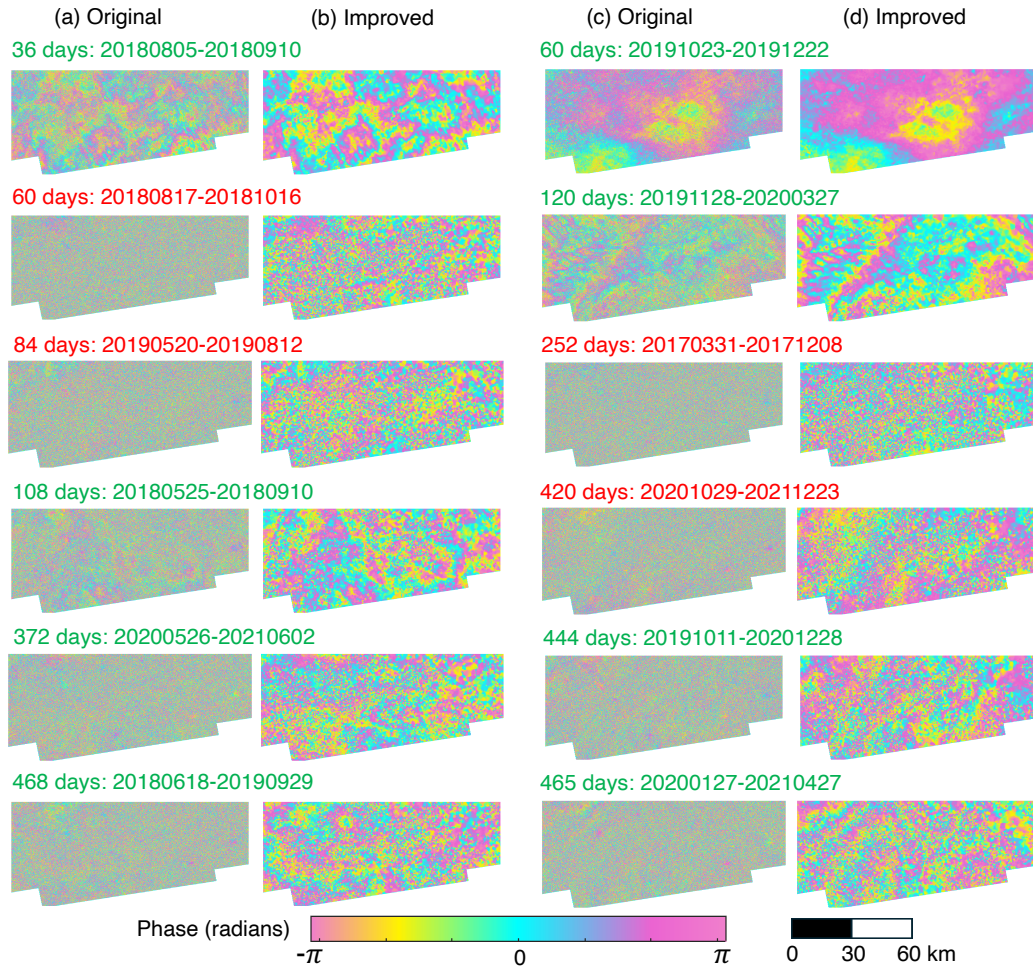


Figure 2. Examples of original interferograms (columns a and c) and reconstructed interferograms (columns b and d) over the Eagle Ford region with varying temporal baselines. Columns a and b use summer Sentinel-1 acquisitions, while columns c and d use Sentinel-1 winter acquisitions. The reconstructed interferograms marked in green were included in the final subset for time series analysis, and the interferograms marked in red were discarded due to relatively large phase unwrapping errors.

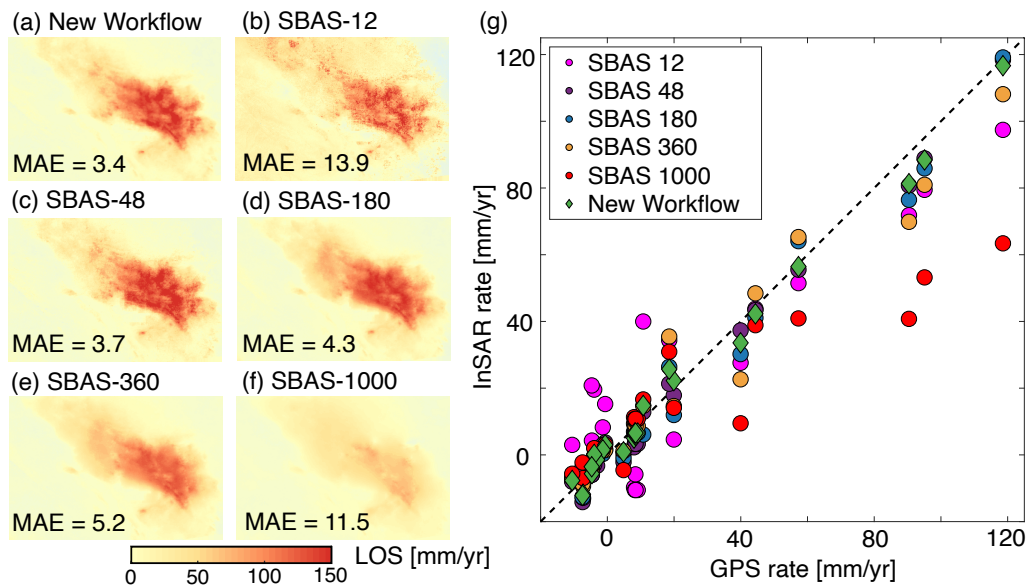


Figure 3. Cumulative line-of-sight (LOS) deformation over the Tulare Basin from 2017-2021 as derived from: (a) a subset of phase reconstructed interferograms with small phase unwrapping errors; and (b-f) a subset of original interferograms with temporal baseline thresholds of 12, 48, 180, 360, and 1000 days. The mean absolute error (MAE) difference of the linear rate estimate (mm/yr) between 24 InSAR and GPS stations over the time period is marked on each deformation solution. Subsidence causes positive LOS deformation (red). (g) Scatter plots of co-located GPS and InSAR LOS deformation rate estimates (mm/yr) derived from different interferogram subsets.

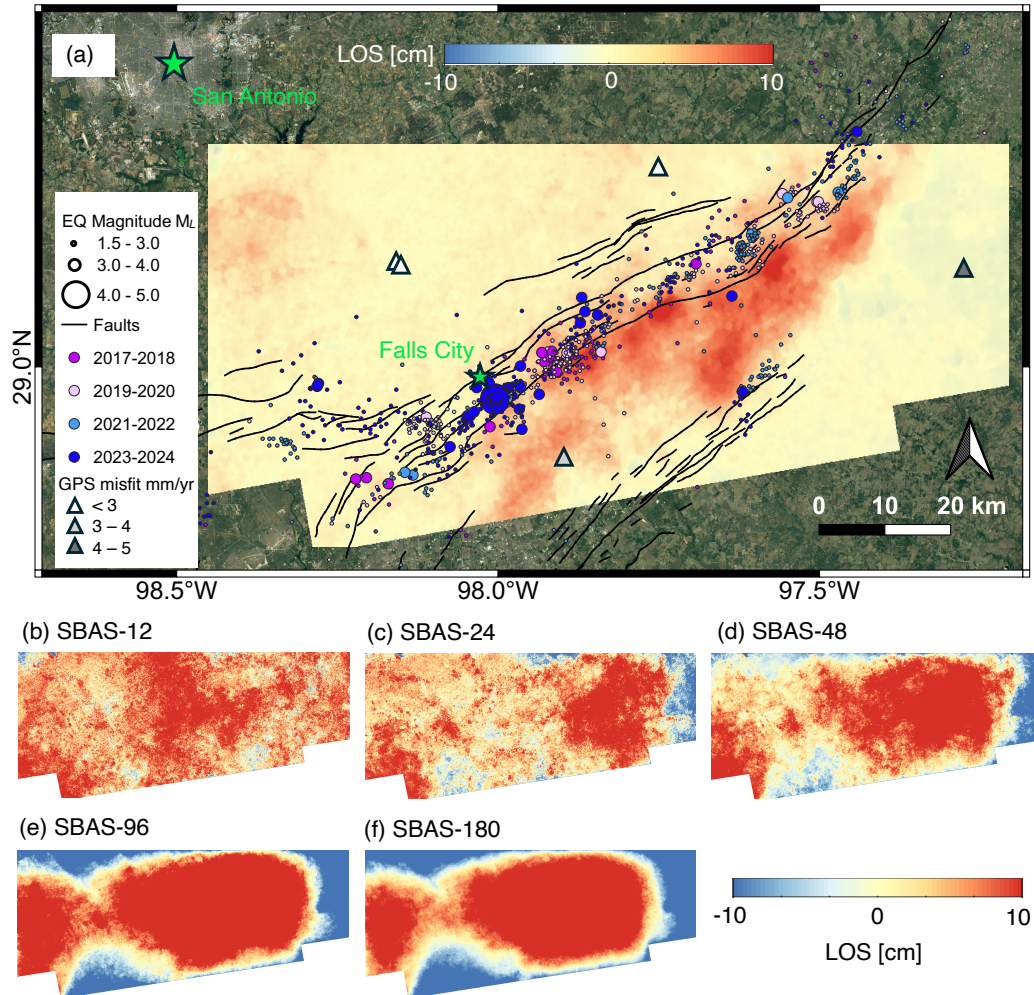


Figure 4. Cumulative line-of-sight (LOS) deformation over the Eagle Ford region between February 2017–December 2021 as derived from: (a) a subset of phase reconstructed interferograms with small phase unwrapping errors. Subsidence leads to positive LOS deformation. The locations and magnitudes of earthquakes since 2017 (circles), mapped faults are from McKeighan et al. (2022), and GPS stations (triangles). A cluster of recent earthquakes ($M_L > 4.0$) occurred near Falls City; and (b-f) original decorrelated interferograms with temporal baseline thresholds of 12, 24, 48, 96, and 180 days.